J. Fluid Mech. (1994), *vol.* 266, *pp.* 277–302

Propagating Holmboe waves at the interface between two immiscible fluids

By O. POULIQUEN, J. M. CHOMAZ AND P. HUERRE
Laboratoire d'hydrodynamique (LadHyX, URA 317), Ecole Polytechnique, F-91128 Palaiseau, France

(Received 11 December 1992 and in revised form 11 October 1993)

The instability of the surface of discontinuity separating two streams of immiscible constant-density fluids is studied experimentally and theoretically near onset when surface tension effects are significant. Following Thorpe's original idea, a tube filled with two immiscible fluids is tilted at an angle and returned to its horizontal position to produce a nearly constant velocity difference between both streams that can be varied continuously across threshold. In order to control the wavenumber near onset, the flow is spatially forced by periodically distributing small obstacles on the upper side of the tank. When the kinematic viscosities of each fluid are nearly equal, ones observes two counter-propagating waves of equal amplitude, which cannot be explained from a vortex sheet model. A linear stability analysis of a density discontinuity embedded within a piecewise-linear velocity profile demonstrates that such waves are Holmboe modes associated with the diffusive layers above and below the interface. Good agreement is obtained between the measured and predicted values of the critical velocity difference, propagation velocity and growth factors of the waves. The instability analysis of the asymmetric velocity profile reveals that the breaking of reflectional symmetry gives rise to a single propagating wave near onset. When the kinematic viscosities of each fluid differ, the first destabilized wave is observed to propagate in the same direction as the less-viscous fluid, in agreement with the theoretical results, and the dominant direction of propagation can be manipulated by adjusting the viscosities accordingly.

1. Introduction

In this combined analytical and experimental study, the onset of the first instability at the interface between two statically stable fluids in relative shearing motion is examined when surface tension effects are significant. A qualitative and quantitative comparison is presented between the predictions of linear stability theory and experimental observations in a tilting tank apparatus.

A shear layer is typically produced by bringing into contact two streams of the same constant-density fluid travelling at different streamwise velocities. In this simple configuration, the resulting velocity profile is known to be subjected to an inflexional instability mechanism, which gives rise to the formation of vortical structures or Kelvin–Helmholtz billows travelling at approximately the average velocity between the two streams (see Ho & Huerre 1984 for a review). If a statically stable continuous stratification is introduced, either by varying the temperature or, in the case of miscible fluids, the concentration of one of the constituents, two essentially different configurations must be distinguished. When the characteristic thicknesses of the density profile d_ρ^* and velocity profile d_u^* are of the same order of magnitude, the

primary instability is the continuation of the Kelvin–Helmholtz instability so that above a critical value of the bulk Richardson number, the basic profile becomes stable (see, for instance, Maslowe & Kelly 1971; Maslowe & Thomson 1971; Hazel 1972). As first demonstrated by Holmboe (1962), the situation is somewhat more complex if the thicknesses d_ρ^* and d_u^* are such that $d_\rho^* \ll d_u^*$. When a density discontinuity is embedded within a piecewise-linear velocity profile, there may exist an additional pair of unstable travelling waves or *Holmboe modes* which have equal and opposite propagation speeds in a frame of reference moving at the average velocity between the two streams. Whereas Kelvin–Helmholtz modes are stationary in the same frame and are only unstable at low values of the Richardson number, travelling modes persist above the neutral boundary of the Kelvin–Helmholtz modes for all values of the Richardson number. These results have subsequently been corroborated by several linear stability analyses of continuous density and velocity profiles with sufficiently sharp density variations (Hazel 1972; Howard & Maslowe 1973; Smyth, Klaasen & Peltier 1988; Smyth & Peltier 1989, 1990). The nonlinear two-dimensional development of Holmboe waves has also been investigated numerically by Smyth *et al.* (1988), and some of the three-dimensional linear instabilities which finite-amplitude Holmboe waves might be subjected to, have recently been documented by Smyth & Peltier (1991).

Relatively few experimental investigations of the instabilities arising in stratified mixing layers have been undertaken (see, for instance, the survey of Maxworthy & Browand 1975), and most of them pertain to spatially evolving stratified shear layers generated downstream of a splitter plate. This configuration has been studied in particular by Scotti & Corcos (1972) and Delisi & Corcos (1973), in the case where d_ρ^* and d_u^* are of equal magnitude and the basic flow is only subjected to the Kelvin–Helmholtz instability. Experimental evidence for the existence of Holmboe waves was first reported in spatial mixing layers with $d_\rho^* \ll d_u^*$ by Browand & Winant (1973) and Koop & Browand (1979). The evolution of interfacial waves and their subsequent breakup at the crests were carefully documented. The present study follows the spirit of the combined analytical and experimental investigation of Kelvin–Helmholtz and Holmboe waves by Lawrence, Lasheras & Browand (1987), and Lawrence, Browand & Redekopp (1991). In these recent studies, the results derived from the temporal linear stability analysis of a broken-line velocity profile presenting a density discontinuity were compared with experimental observations in spatially evolving stratified mixing layers. Striking visualizations of the transition between the Kelvin–Helmholtz and Holmboe regimes were obtained but, according to these authors, the initial profile asymmetry behind the splitter plate made it difficult to carry out a detailed quantitative analysis of the dynamics of counter-propagating Holmboe waves. Following Reynolds original idea (1883), Thorpe (1968) ingeniously devised a temporal mixing-layer configuration by tilting at an angle a tank filled with either two immiscible fluids (Thorpe 1969), or a stably stratified fluid mixture (Thorpe 1973*a*, *b*). For the most part attention was focused on the evolution of Kelvin–Helmholtz billows in the case of continuous stratification with $d_\rho^* \approx d_u^*$.

In the present investigation, we adopt the same experimental set-up as in Thorpe (1968), but we choose to concentrate exclusively on the spatio-temporal dynamics of the interface separating two immiscible fluids. Thus, in contrast to spatially developing mixing layers, the basic flow is uniform in the stream direction. Furthermore we only examine the initiation of unstable motion close to onset. As opposed to the earlier study of Pouliquen *et al.* (1992), the tilting tank is returned to its horizontal position to produce, beyond an initial accelerating phase, a nearly constant velocity difference across the interface which can be varied continuously above and below threshold. In

this flow regime, surface tension effects play a crucial role in determining the critical value of the velocity difference and they have to be included in any model of the resulting instability. The basic flow close to threshold is unstable to a continuous band of wavenumbers that may lead, in such a spatially extended system, to complex spatio-temporal regimes. A unique feature of the present experimental setup is the presence of periodic spatial forcing in the form of small obstacles distributed along one of the walls of the tube. As demonstrated in Pouliquen *et al.* (1992), this technique is very effective in locking the interface deformation to a particular wavenumber. In this manner, the response of the flow to a well-defined wavenumber can be analysed. Finally, the aspect ratio of the tube is chosen large enough that the instability is primarily two-dimensional, i.e. the interface elevation does not vary appreciably in the cross-stream direction and the three-dimensional instabilities described by Smyth & Peltier (1990, 1991) are quenched. As in Lawrence *et al.* (1991), the experimental observations and measurements are compared to the predictions of linear temporal instability analysis applied to a broken-line profile containing a sharp density interface. But, in contrast to this earlier investigation, surface tension effects are necessarily included. It should be emphasized that the slope discontinuities appearing in the piecewise-linear velocity profile do not lead to spurious instability characteristics when compared to continuous velocity distributions, as convincingly shown by Balsa (1987). The present theoretical analysis extends earlier results derived by Thorpe (1969) for symmetric velocity profiles.

The paper is organized as follows. The experimental set-up and procedure are briefly presented in §2 and preliminary observations in §3. The combined theoretical–numerical study is described in detail in §4. For ease of presentation, the properties and predictions of the symmetric model (§§4.1 and 4.2) and asymmetric model (§§4.3 and 4.4) are examined separately. Finally, the main results of the study are summarized in §5.

In what follows starred and unstarred quantities denote dimensional and non-dimensional variables respectively.

2. Experimental set-up and procedure

The experimental configuration of Thorpe (1968, 1969, 1973*a*, *b*) has been chosen in order to generate a shear that is spatially uniform in the streamwise direction (figure 1). As in Pouliquen *et al.* (1992), a cylindrical glass tube of circular cross-section which is 2 m long and 6 cm in diameter is filled with two immiscible fluids with respective viscosities μ_1^* and μ_2^*, and respective densities ρ_1^* and ρ_2^* with $\rho_1^* > \rho_2^*$. When the tank is tilted at an angle $\alpha(t^*)$ from its initially horizontal position, the two fluid layers move in opposite directions with respective velocities $U_1^*(t^*)$ and $U_2^*(t^*)$. In the present experiments different sets of fluids have been used. Set 1 is made up of water and of an equal mixture of silicon oil (47V2) and 1-2-3-4-tetrahydronaphtalene. Sets 2 and 3 are made up of a mixture of kerosene and silicone oil V100, and a mixture of 80% alcohol and 20% water. The physical properties of these fluid pairs are summarized in table 1. Viscosities are measured using a falling-ball-type viscosimeter, and surface tension is determined by the pendant drop method. In order to generate a shear layer with equal and opposite free-stream velocities $U_2^*(t^*) = -U_1^*(t^*) \equiv U^*(t^*)$, both fluid layers are chosen to be of equal depth throughout the investigation.

In the study reported by Pouliquen *et al.* (1992), the inclination angle α was maintained at a constant value α_m in order to create a uniform accelerating shear. The resulting basic flow then became unstable at the critical time when the instantaneous

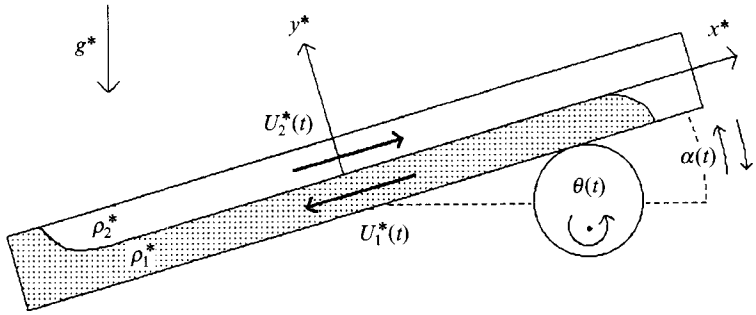

FIGURE 1. Experimental set-up: a tank filled with two fluids of density ρ_1^* and ρ_2^* is inclined at an angle α_m and brought back to its horizontal position in a single rotation of the cam $0 < \theta \leqslant 2\pi$.

	Fluid	Density ($g\,cm^{-3}$)	Viscosity (cP)	Surface tension ($mN\,m^{-1}$)	β
Set 1	Water	$\rho_1^* = 1.0$	$\mu_1^* = 1.0$	$\gamma^* = 80$	0.14
	Equal mixture of silicone oil V2 and 1-2-3-4-tetrahydronaphtalene	$\rho_2^* = 0.92$	$\mu_2^* = 1.9$		
Set 2	Mixture of 80% alcohol and 20% water	$\rho_1^* = 0.848$	$\mu_1^* = 2.1$	$\gamma^* = 5.2$	7×10^{-3}
	Mixture of 12% silicone oil V100 and 88% kerosene	$\rho_2^* = 0.796$	$\mu_2^* = 2.3$		
Set 3	Mixture of 80% alcohol and 20% water	$\rho_1^* = 0.848$	$\mu_1^* = 2.1$	$\gamma^* = 5.3$	-0.09
	Mixture of 7% silicone oil V100 and 93% kerosene	$\rho_2^* = 0.784$	$\mu_2^* = 1.6$		

TABLE 1. Physical properties of the fluids used in the experiments. The dimensionless asymmetry parameter β is defined by equation (1)

velocity difference $\Delta U^*(t^*) \equiv U_2^*(t^*) - U_1^*(t^*)$ exceeded a critical value ΔU_c^*. The rapid increase of $\Delta U^*(t^*)$ beyond the threshold value ΔU_c^* subsequently resulted in large interfacial deformations. In the present experiment, one seeks to produce a basic flow where the velocity difference can be conveniently maintained at a constant value ΔU_m^* close to onset. Accordingly, the tube is initially tilted at an angle α_m during an accelerating phase, to create a chosen velocity difference ΔU_m^*, and it is then returned to its horizontal position $\alpha = 0$ to keep ΔU^* constant and equal to ΔU_m^*. In this mode of operation, there is a clearly identifiable control parameter, namely ΔU_m^*, and it can be varied continuously across the threshold value ΔU_c^*.

The time history $\alpha(t^*)$ of the inclination angle is specified by means of a motor of angular velocity ω^*, which drives an eccentric cam as sketched in figure 1. With a full rotation of the cam, the angle α increases from zero, reaches its maximum value α_m and then returns to zero. The corresponding velocity in each fluid layer is given by

$$U_2^*(t^*) = -U_1^*(t^*) = U^*(t^*) = \int_0^{t^*} \frac{\rho_1^* - \rho_2^*}{\rho_1^* + \rho_2^*} g^* \sin(\alpha(t^*))\, \mathrm{d}t^*,$$

where g^* denotes gravity. Noting that α is in fact a function of the rotation angle of the cam θ which varies in the range $0 < \theta \leqslant 2\pi$, one may write for the final velocity U_m^*:

$$U_m^* = \frac{1}{\omega^*} \frac{\rho_1^* - \rho_2^*}{\rho_1^* + \rho_2^*} g^* \int_0^{2\pi} \sin(\alpha(\theta))\, \mathrm{d}\theta.$$

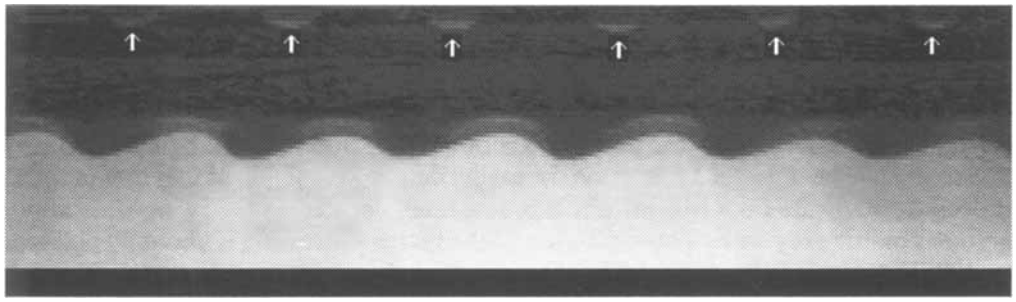

FIGURE 2. Interface deformation 2 s after the onset of instability. Fluid set 2, $\Delta U_m^* = 16$ cm s^{-1}, $\lambda_f^* = 3.7$ cm; note the location of the periodically distributed obstacles at the top boundary as indicated by the arrows.

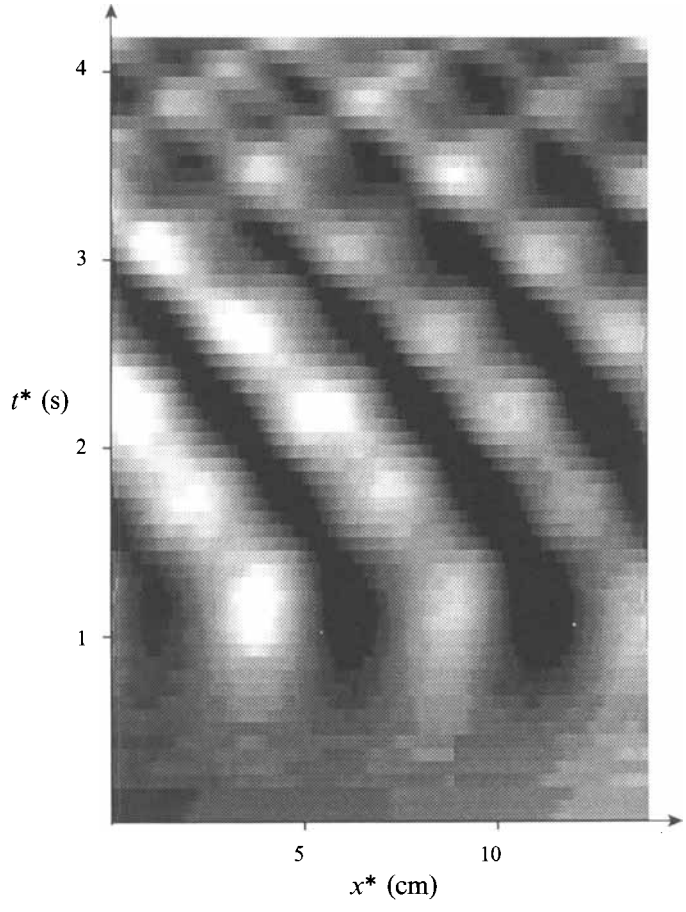

FIGURE 3. Spatio–temporal x^*–t^* diagram of interface deformation. Fluid set 1, $\Delta U_m^* = 24$ cm s^{-1}, $\lambda_f^* = 5$ cm; darker (lighter) regions indicate the crest (troughs) of the interface deformation. The tube is brought back to its horizontal position at $t^* = 1$ s.

Thus, one is able to control the final velocity difference $\Delta U_m^* = 2U_m^*$ between the fluid layers simply by varying the rotation rate of the motor ω^*. A typical experimental run lasts 3–4 s. The duration of the experiment is limited by the hydraulic jumps which propagate towards the centre of the tube from the ends.

To visualize the interface, fluorescein dye is mixed with the heavier fluid and a laser sheet is created in the vertical plane containing the axis of the tube. The resulting pictures are recorded on film with a CCD movie camera. A typical photograph is shown on figure 2, where the interface appears as the boundary between the illuminated heavier fluid in the bottom part of the tube and the dark lighter fluid in the upper part. The interface elevation is easily determined by making use of image processing software on a Macintosh. It is accurately located as the point of maximum gradient on the grey scale. The resolution of the image processing is about 30 pixels per cm. The interface deformation can then be recorded and images are digitized in order to measure its position. The spatio–temporal dynamics of the interface can be summarized on an x^*–t^* diagram as shown on figure 3. At each time step, the interface has been represented by a line along the x-axis, the grey level at each point being related to the corresponding elevation of the interface (white in a trough, black on a crest). The propagative nature of the interface deformation is clearly apparent, as discussed in the next section.

As in Pouliquen *et al.* (1992) the flow is spatially forced at a specific wavelength by periodically placing 3 mm high metallic obstacles on the upper wall of the tube (figure 2). These are maintained in position with movable magnets distributed along the outer wall of the tube. Pouliquen *et al.* have established that when the forcing wavelength stays close to the natural wavelength of the instability, the interface response is locked, i.e. it is perfectly periodic at the forcing wavelength. In the present context this property of the flow is essential: a single wavelength can be isolated and its temporal dynamics observed close to onset. By forcing the flow at a fixed wavelength more complex spatio–temporal behaviour is completely inhibited.

3. Preliminary experimental observations

The initial experiments were conducted with the first set of fluids (table 1). A typical spatio–temporal x^*–t^* diagram for the elevation of the interface is displayed on figure 3 when the velocity difference ΔU_m^* is close to ΔU_c^*. The interface, which is flat at $t^* = 0$ s, is initially deformed into a *stationary* sinusoidal pattern at the forcing wavelength. This stationary growth process terminates at around $t^* = 1.4$ s and it is followed by a propagating regime where the interface sustains travelling waves which move predominantly to the left in the same direction as the lower fluid. The fundamental wavelength does not seem to be affected by the propagation. However, significant changes are noticeable in the amplitude variations. The black pulses appearing on figure 3 for $t^* > 1.4$ s seem to indicate temporally periodic amplitude modulations. A closer examination reveals that such modulations are due to the presence of a counter-propagating wave of smaller amplitude moving to the right in the same direction as the upper fluid layer.

Two types of instability could lead to the deformation of the interface: the Tollmien–Schlichting and Kelvin–Helmholtz instabilities. The first one is of viscous type, and grows over viscous timescales, typically equal to the ratio of the square of the thickness of the boundary layer to the kinematic viscosity. In our experiments, this timescale is about 20 s and it is much larger than the characteristic time observed on figure 3 for the growth of the waves. The instability of interest here is actually of an inviscid nature, and belongs to the Kelvin–Helmholtz class.

The simplest theoretical model one can think of to describe the initial evolution of the interface is the classical vortex sheet (Drazin & Reid 1981) separating two immiscible fluids of respective density ρ_1^* and ρ_2^* with $\rho_1^* > \rho_2^*$, moving at constant and

opposite speeds, the velocity in each fluid being uniform. In the presence of surface tension, the sheet is found to be unstable to stationary disturbances above a critical value

$$\Delta U_c^* = \left(2\frac{\rho_1^*+\rho_2^*}{\rho_1^*\rho_2^*}((\rho_1^*-\rho_2^*)g^*\gamma^*)^{\frac{1}{2}}\right)^{\frac{1}{2}},$$

where γ^* is the surface tension coefficient. Thorpe (1969) obtained good quantitative agreement between experimental observations in accelerated flow and theoretical predictions based on the vortex sheet model for the threshold value ΔU_c^* and the initial growth rate σ^* of the perturbations. This result demonstrates that the presence of diffusive layers at the interface can indeed be neglected in the accelerating flow configuration. In the present nearly constant ΔU^* case, the theoretical value $\Delta U_c^* = 0.185\ \mathrm{m\ s^{-1}}$ for fluids of set 1 compares favourably with the experimental one $\Delta U_c^* = 0.195\ \mathrm{m\ s^{-1}}$, but the measured growth rate $\sigma^* = 3.1\ \mathrm{s^{-1}}$ is far below the theoretical value $\sigma^* = 15.6\ \mathrm{s^{-1}}$. More crucially, the linear stability analysis of the vortex sheet completely fails to account for the observed propagative features. In order to include propagative effects, one must consider a more realistic velocity profile that is continuous at the interface.

4. Linear stability analyses; comparison with experiments

The vortex sheet analysis is abandoned in favour of a continuous velocity model where the diffusive layers on either side of the interface are explicitly taken into account. Following Lawrence *et al.* (1991), the basic flow sketched on figure 4 is introduced. Two streams of infinite height and respective densities ρ_1^* and ρ_2^* ($\rho_1^* > \rho_2^*$) and velocities $-U^*$ and U^* are separated at $y^* = 0$ by a density interface with surface tension γ^*. The diffusive layers of respective thicknesses d^* and δd^* in the upper and lower fluids are modelled by a piecewise-linear velocity profile. The case $\delta = 1$ has been studied by Thorpe (1969). The fluid velocity at the interface is continuous and taken to be equal to a fraction βU^* of the free-stream velocity U^*. The dimensionless parameters δ and β provide a measure of the asymmetry of the velocity profile. They can be related to the properties of each fluid by the following reasoning. If one assumes that the velocity profile is created through viscous diffusion by setting the two fluids into motion at time $t^* = 0$, the characteristic thickness of the diffusive layers evolves according to the laws $d^* \sim (\nu_2^* t^*)^{\frac{1}{2}}$ and $\delta d^* \sim (\nu_1^* t^*)^{\frac{1}{2}}$ respectively, where ν_1^* and ν_2^* denote the kinematic viscosities. Thus, δ is simply given by

$$\delta = (\nu_1^*/\nu_2^*)^{\frac{1}{2}}.$$

Furthermore, imposing that the shear stress be continuous at the interface $y^* = 0$ provides the following relation between δ and β:

$$\beta = \frac{1-\delta\rho_1^*/\rho_2^*}{1+\delta\rho_1^*/\rho_2^*}. \tag{1}$$

The linear stability analysis is performed under the assumption that the basic flow is quasi-steady, i.e. it evolves on a diffusive timescale that is much longer than the characteristic timescale of the instability. Furthermore viscous effects are included to properly define the velocity profile, as discussed above, but they are ignored in the perturbation analysis. In other words, one only considers the inviscid stability of the flow defined in figure 4. Dimensionless unstarred variables are introduced based on the free-stream velocity U^*, the capillary length $L^* = (\gamma^*/[g^*(\rho_1^*-\rho_2^*)])^{\frac{1}{2}}$ and the density

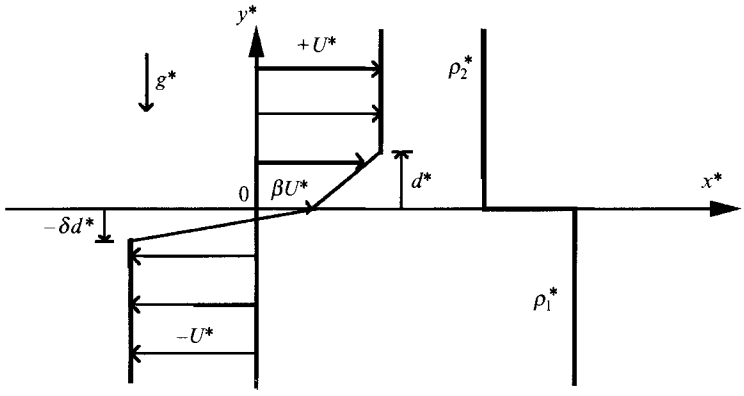

FIGURE 4. Sketch of basic flow for the linear stability analysis of §4.

scale $\rho_1^*+\rho_2^*$. The linear stability properties are then a function of four dimensionless parameters:

the dimensionless thickness of the upper diffusion layer $d = d^*/L^*$,

the asymmetry parameter β,

the density ratio $\rho_1 = \rho^*/(\rho_1^*+\rho_2^*)$,

the modified Richardson number $J = (\rho_1^*-\rho_2^*)g^*L^*/[(\rho_1^*+\rho_2^*)U^{*2}]$, which is the primary control parameter of the instability. Recall that the asymmetry parameter δ is directly related to β through (1).

The classical Richardson number is usually defined with respect to a typical lengthscale d^* of the shear-layer velocity profile. Note that, in the present context, we have introduced instead the unconventional 'modified Richardson number' J based on the capillary lengthscale L^*, as in earlier studies of the vortex sheet model (Thorpe 1969, p. 29). With such a choice of dimensionless parameters, the effect of the velocity difference ΔU^* is contained in J while the effect of finite thickness d^* is confined to the parameter d. Thus, one may study the transition from the continuous velocity profile to the vortex sheet simply by letting d go to zero at a constant value of J.

Small two-dimensional perturbations of the form $\Phi(y)\exp[ik(x-ct)]$ are governed by the Rayleigh equation

$$\frac{\mathrm{d}^2\Phi}{\mathrm{d}y^2}-k^2\Phi-\frac{\mathrm{d}^2U}{\mathrm{d}y^2}\frac{1}{U-c}\Phi = 0,$$

where k is the real wavenumber and c the complex phase velocity. The unknown eigenfunction Φ is subjected to the usual continuity of displacement conditions at $y = d$, $y = 0$ and $y = -\delta d$, namely,

$$\left[\frac{\Phi}{U(y)-c}\right]_{y=0-}^{y=0+} = \left[\frac{\Phi}{U(y)-c}\right]_{y=d-}^{y=d+} = \left[\frac{\Phi}{U(y)-c}\right]_{y=-\delta d-}^{y=-\delta d+} = 0.$$

Continuity of pressure at $y = d$ and $y = -\delta d$, and the jump in pressure due to surface tension acting on the interface $y = 0$ provide the additional conditions:

$$\left[(U(y)-c)\frac{\mathrm{d}\Phi}{\mathrm{d}y}-\frac{\mathrm{d}U}{\mathrm{d}y}\Phi\right]_{y=d-}^{y=d+} = 0,$$

$$\left[(U(y)-c)\frac{\mathrm{d}\Phi}{\mathrm{d}y}-\frac{\mathrm{d}U}{\mathrm{d}y}\Phi\right]_{y=-\delta d-}^{y=-\delta d+} = 0,$$

$$\left[\rho(y)\left((U(y)-c)\frac{\mathrm{d}\Phi}{\mathrm{d}y}-\frac{\mathrm{d}U}{\mathrm{d}y}\Phi\right)\right]_{y=0-}^{y=0+} = J\left[\frac{\Phi}{U-c}\right]_{y=0}(1+k^2). \qquad (2)$$

In what follows, we shall make the Boussinesq approximation: density variations will only be considered in the buoyancy term involving J on the right-hand side of (2). In all remaining terms, we shall set $\rho_1^* = \rho_2^*$ so that $\rho(y) = \frac{1}{2}$ on the left-hand side of (2). The assumption amounts to choosing $\rho_1 = \frac{1}{2}$ for the dimensionless density ratio. Note also that relation (1) between β and δ then reduces to

$$\delta = \frac{1-\beta}{1+\beta}. \tag{3}$$

Solving the Rayleigh equation and imposing all jump conditions above and the usual exponential decays at $y = \pm\infty$ then leads to the dispersion relation:

$$c^4 + n_3 c^3 + n_2 c^2 + n_1 c + n_0 = 0, \tag{4}$$

where

$$n_3 = -2\beta,$$

$$n_2 = -\left(J\frac{1+k^2}{k} + \frac{2\beta^2}{(1-\beta)kd}\right) + \frac{2\beta}{(1-\beta)kd}\left(\frac{1+e}{f} + \frac{1+g}{h}\right) - \frac{1-eg}{hf} - 2\beta\left(\frac{e}{f} + \frac{g}{h}\right) + \beta^2,$$

$$n_1 = -\left(J\frac{1+k^2}{k} + \frac{2\beta^2}{(1-\beta)kd}\right)\left(\frac{1+e}{f} + \frac{1+g}{h}\right) + \frac{2\beta}{(1-\beta)kd}\frac{(1+e)(1+g)}{hf} + \frac{2\beta(1-eg)}{hf} + \beta^2\left(\frac{e}{f} + \frac{g}{h}\right),$$

$$n_0 = -\left(J\frac{1+k^2}{k} + \frac{2\beta^2}{(1-\beta)kd}\right)\frac{(1+e)(1+g)}{hf} - \frac{\beta^2(1+eg)}{hf},$$

with e, f, g and h denoting the following quantities:

$$e = \left(\frac{2(1-\beta)kd}{(1+\beta)^2} - 1\right)\exp\left(2\frac{1-\beta}{1+\beta}kd\right), \quad f = \frac{2(1-\beta)kd}{(1+\beta)^2}\exp\left(2\frac{1-\beta}{1+\beta}kd\right),$$

$$g = \left(\frac{2kd}{1-\beta} - 1\right)\exp(2kd), \quad h = -\frac{2kd}{1-\beta}\exp(2kd).$$

The dispersion relation is a fourth-order polynomial in c, with coefficients depending on k and the control parameters d, β, and J. In the following subsections, the cases of symmetric and asymmetric velocity profiles are separately examined.

4.1. *Symmetric velocity profile: theoretical results*

When $\beta = 0$, the fluid velocity at the interface is zero and, according to (3), $\delta = 1$. In this situation, both fluids have identical kinematic viscosities and the velocity profile sketched on figure 4 is odd, with the same thickness for the diffusive layers in each fluid. The dispersion relation (4) then reduces to the equation

$$c^4 + n_2 c^2 + n_0 = 0, \tag{5}$$

with $$n_2 = -J\frac{1+k^2}{k} + \frac{e^{-4kd} - (2kd-1)^2}{4k^2d^2}, \quad n_0 = J\frac{1+k^2}{k}\frac{(e^{-2kd} + 2kd - 1)^2}{4k^2d^2}.$$

The case of an interface with surface tension embedded within a symmetric velocity profile was originally studied by Thorpe (1969). The dispersion relation (5) is indeed identical to equation (2.33) of that paper. While Thorpe examined the influence of thin

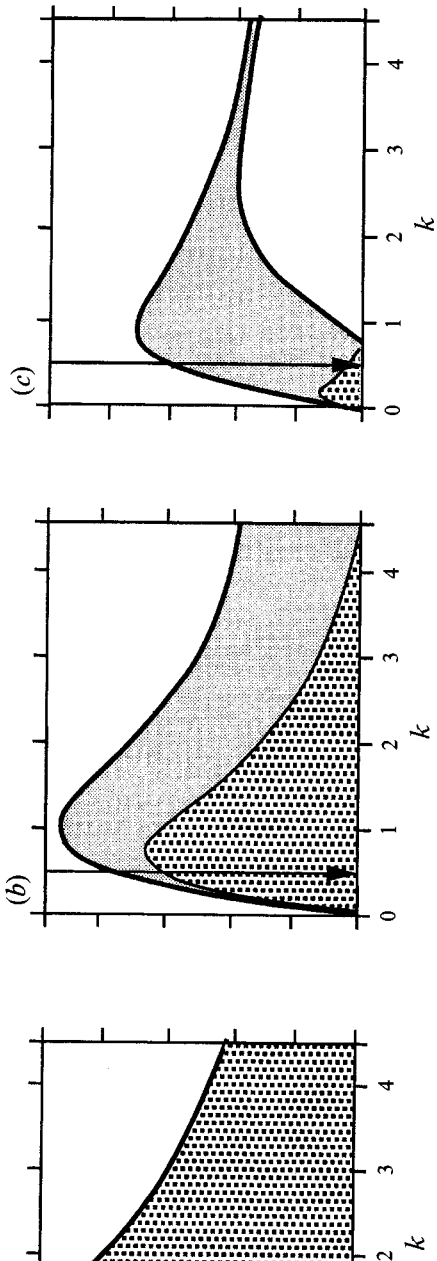

FIGURE 5. Stability diagram of piecewise-linear model in the (wavenumber k, Richardson number J)-plane for different values of the thickness parameter d. Asymmetry parameter β is set equal to zero. Clear region: neutrally stable modes ($c_i \neq 0$; $c_i = 0$); dotted regions: stationary unstable Kelvin–Helmholtz modes ($c_r = 0$; $c_i > 0$); shaded regions: counter-propagating unstable Holmboe modes ($c_r \neq 0$; $c_i > 0$); thicker curve: marginal stability boundary. (*a*) $d = 0$; (*b*) $d = 0.1$; (*c*) $d = 1$.

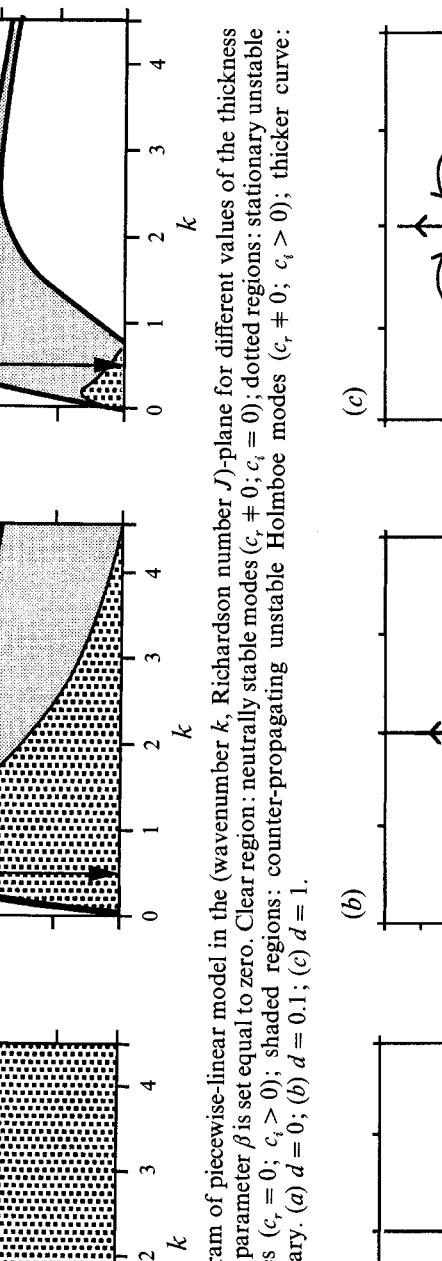

Figure 6. Loci of eigenvalues in the complex (c_r, c_i)-plane as Richardson number J is decreased along the vertical path indicated on figure 5, for different values of thickness parameter d: (*a*) $d = 0$; (*b*) $d = 0.1$; (*c*) $d = 1$. Arrows indicate the direction of migration of the eigenvalues as J is lowered.

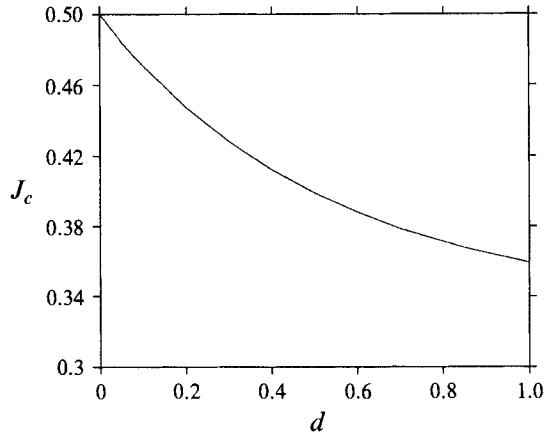

FIGURE 7. Critical Richardson number J_c as a function of thickness parameter d.

diffusive layers on the critical values ΔU_c and k_c of the velocity difference and wavenumber, we focus attention instead on the propagative or stationary nature of the unstable modes within the marginal stability curve and examine the transition from the continuous velocity profile to the vortex sheet in the limit $d \to 0$.

As in all purely inviscid stability analyses, the eigenvalues appear in complex-conjugate pairs and the flow becomes unstable if one of the roots of (5) is complex. Furthermore, if c is a solution, $-c$ is also a solution, as a result of the symmetry of the velocity profile. The temporal stability properties of the basic flow (k real, c complex) are summarized on figures 5, 6 and 7, as a function of the two remaining dimensionless variables, namely the scaled thickness d and modified Richardson number J. For specific values of d, the various domains of instability are indicated by dotted and shaded regions in the (k, J)-plane on figure 5. The upper curve is the marginal stability boundary between the neutrally stable clear region where all four eigenvalues are real, and the unstable regions where all four eigenvalues are complex. In the dotted areas the eigenvalues are all purely imaginary and correspond to *stationary* modes, whereas in the shaded areas they are complex with non-zero real parts and correspond to *propagating* modes. When a particular path is followed in the (k, J)-plane as specified on figure 5, the eigenvalues move along curves in the complex (c_r, c_i)-plane as depicted on figure 6. Finally, the value of the critical modified Richardson number J_c at the maximum of the marginal stability curve is plotted against the thickness parameter d on figure 7.

The case $d = 0$ corresponds to the classical Kelvin–Helmholtz instability of the vortex sheet separating two uniform streams in the presence of surface tension (Drazin & Reid 1981). According to figure 5(*a*), the flow is neutrally stable when $J > 0.5$ and unstable when $J < 0.5$. Furthermore, all growing perturbations are *stationary Kelvin–Helmholtz modes* with $c_r = 0$. When a diffusive layer of scaled thickness $d = 0.1$ is introduced, as in figure 5(*b*) the first instability that appears at onset is no longer stationary but propagative with $c_r \neq 0$. In continuously stratified shear flows where the density layer is much thinner than the velocity layer, such propagating disturbances have been well documented (Holmboe 1962; Hazel 1972; Browand & Winant 1973; Howard & Maslowe 1973; Smyth *et al.* 1988; Smyth & Peltier 1989, 1990, 1991; Lawrence *et al.* 1991). Following these authors, propagating perturbations of the interface are also referred to, in the present case, as *Holmboe modes*. It should be noted, however, that significant differences exist between the properties of Holmboe waves in

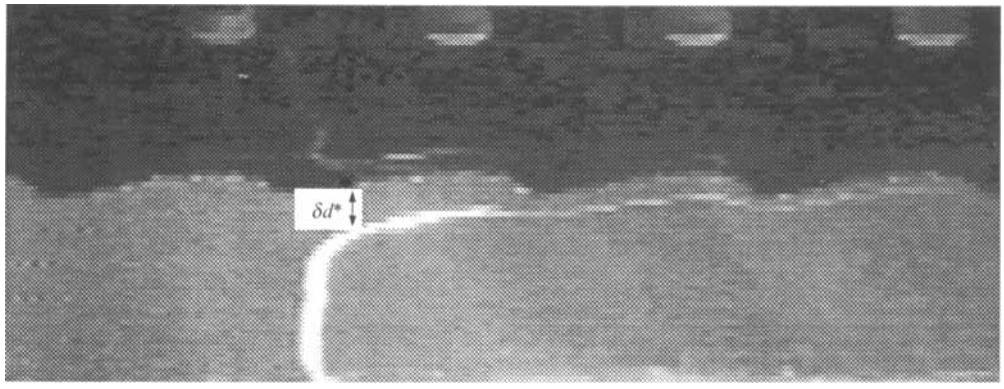

FIGURE 8. Visualization of velocity profile in lower fluid. A vertical dye line is deposited immediately before tilting the tank and its subsequent deformation is recorded. The thickness $\delta d^*(t^*)$ is determined as the maximum slope thickness of the retrieved profile. Fluid set 2, $\Delta U_m^* = 14$ cm s^{-1}, $\lambda_f^* = 3$ cm, $t^* = 2.5$ s.

each situation. In a continuously stratified flow, Holmboe modes exist in a tongue-shaped region that extends to infinity in the wavenumber–Richardson-number plane and the critical value of the Richardson number is pushed to infinity. In the case of immiscible fluids that is of interest here, surface tension acts to dampen large wavenumbers and there is a well-defined value of the threshold J_c. In both instances, stationary Kelvin–Helmholtz modes appear at small values of the control parameter (figure 6*b*).

The transition between these two distinct modes of instability can be understood by following the migration of eigenvalues in the complex (c_r, c_i)-plane as the modified Richardson number J decreases from infinity along the vertical line $k = 0.5$ (figure 6*b*). For large J, all four eigenvalues lie on the real c_r-axis. As the marginal stability boundary in figure 5(*b*) is crossed, they collide two by two at a finite value of c_r on the real axis to produce two complex-conjugate pairs of counter-propagating amplified and decaying Holmboe waves. Finally, as J crosses into the Kelvin–Helmholtz domain on figure 5(*b*), the four eigenvalues experience paired collisions again, but on the imaginary axis, to give rise to two sets of stationary amplified and decaying Kelvin–Helmholtz modes. The eigenvalues remain on the imaginary axis as J is further decreased to zero.

The transition to the classical Kelvin–Helmholtz vortex sheet limit is made obvious by examining the qualitative changes taking place in the stability diagrams (figures 5*c*, 5*b*, 5*a*) and eigenvalue plots (figures 6*c*, 6*b*, 6*a*) as d is decreased to zero. The Kelvin–Helmholtz domain is seen to gradually increase in extent at the expense of the Holmboe domain until the marginal stability boundary coincides with the limiting curve of the Kelvin–Helmholtz region when $d = 0$ (figure 5*a*). Simultaneously, the collision points on the eigenvalue plots approach the origin as d decreases to zero, until one obtains the limiting structure displayed on figure 6(*a*), in agreement with existing weakly nonlinear analyses of vortex sheets (Weissman 1979). Finally, one notes that the finite thickness of the shear layer tends to decrease the critical value of the modified Richardson number J as shown on figure 7.

With a set of dimensionless parameters based on the capillary lengthscale L^*, we have been able to study both the vortex sheet and the continuous velocity profile, and to illustrate how propagative modes appear when diffusive layers at the interface are gradually introduced.

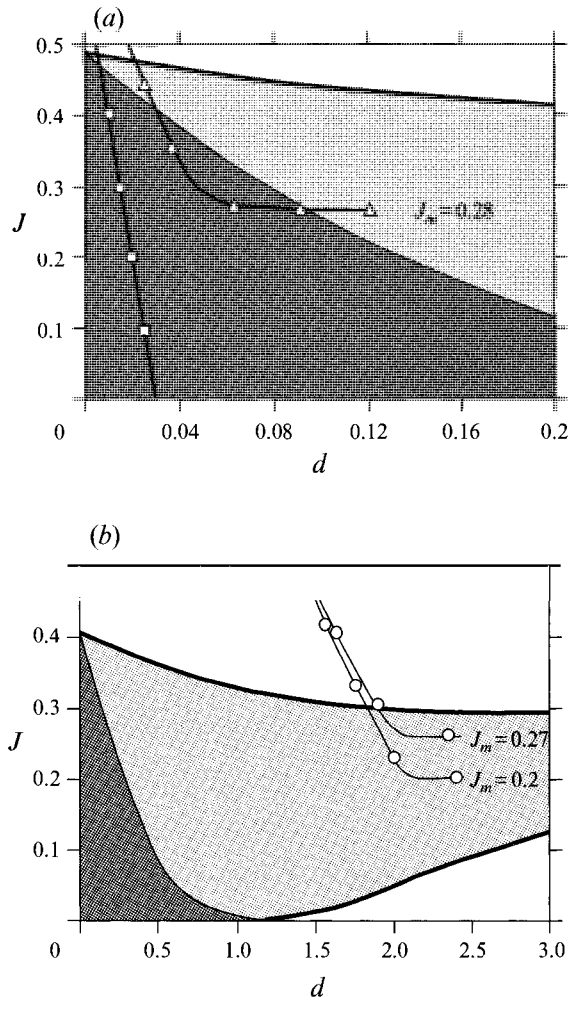

FIGURE 9. Stability diagram of piecewise-linear model in the (thickness d, Richardson number J)-plane at a fixed value of the dimensionless wavenumber k. The clear and shaded regions are defined as in figure 5. (*a*) $k = 1.3$: □, accelerating shear experiment, fluid set 1, $\alpha_m = 15°$; △, constant shear experiment, fluid set 1, $\Delta U_m^* = 24$ cm s^{-1} ($J_m = 0.28$), $\lambda_f^* = 5$ cm. (*b*) $k = 0.54$: ○, constant shear experiment, fluid set 2, $\Delta U_m^* = 14$ cm s^{-1} ($J_m = 0.2$), $\Delta U_m^* = 12$ cm s^{-1} ($J_m = 0.27$), $\lambda_f^* = 3.7$ cm.

4.2. *Symmetric velocity profile: comparison with experiments*

The experimental observations can be interpreted in the light of the previous theoretical results. In order to obtain a complete set of data, two experimental runs are carried out for each value of the velocity difference ΔU_m^*. In the first run, fluorescein dye is mixed in the bulk of the lower fluid to accurately record and measure the elevation of the interface. In the second run, a vertical line of fluorescein dye is produced in the lower fluid immediately before tilting the tube. From the subsequent deformation of the line during the course of the experiment, one can retrieve the instantaneous velocity $-U^*(t)$ of the lower stream and the instantaneous thickness $\delta d^*(t)$ of the corresponding velocity profile as illustrated on figure 8. Since the flow is spatially forced, the wavenumber k is kept constant and each experimental run is represented by a specific path in the (d, J)-plane as shown on figure 9. The dotted (shaded) areas on the figure identify regions of stationary (propagating) modes at a

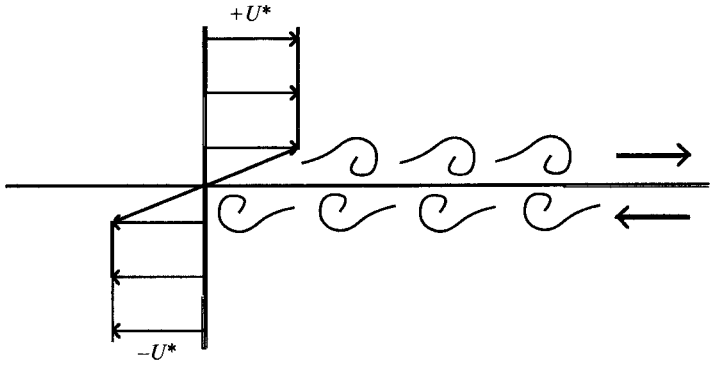

FIGURE 10. Sketch of counter-propagating Holmboe waves and associated vortices.

fixed value of k, as obtained from the stability analysis in the previous section. In the experimental run performed with fluid set 1 and corresponding to the x^*–t^* plot of figure 3, the flow evolves along the curve marked with triangular symbols on figure 9(*a*). As the tube is tilted at an angle α_m and brought back to its horizontal position, the velocity difference ΔU^* initially increases during an accelerating phase from zero to its nominal value $\Delta U_m^* = 2U_m^*$ and subsequently remains nearly constant in time. Correspondingly, the instantaneous modified Richardson number J rapidly decreases from infinity to its nominal value $J_m = (\rho_1^* - \rho_2^*)/(\rho_1^* + \rho_2^*) g^* L^*/U_m^{*2}$ and remains nearly constant thereafter. During this process, diffusive layers are produced on either side of the interface that slowly grow in time. Thus the basic flow may be considered as quasi-steady beyond the initial accelerating phase. The wavenumber k and the modified Richardson number J are then constant and d is the only slowly time-varying parameter. As d becomes sufficiently large a switch from stationary Kelvin–Helmholtz modes to propagating Holmboe modes should be observed. As seen on figure 9(*a*), the characteristics of the basic velocity profile represented by triangles initially lie in the Kelvin–Helmholtz domain and stationary perturbations are indeed observed on figure 3 in the early portion of the run. At the critical time $t^* = 1.4$ s, the basic flow crosses into the Holmboe region on figure 9(*a*) and this is associated with a sudden bending of the rays on figure 3 giving rise to propagating Holmboe waves. A typical path followed in the accelerating shear case where the tube is kept tilted (Thorpe 1969; Pouliquen *et al.* 1992) is indicated by square symbols on figure 9(*a*). The accelerating flow leads to a very rapid decrease in J and relatively slow increase of the scaled thickness d. In contrast to the previous case, the flow therefore remains in the Kelvin–Helmholtz domain for the entire duration of the experiment. Stationary Kelvin–Helmholtz billows are then observed which can be very well described by a linear stability analysis of the temporally evolving vortex sheet ($d = 0$) as demonstrated by Thorpe (1969).

A physical interpretation of the transition between Kelvin–Helmholtz and Holmboe modes has been proposed by Holmboe (1962) and documented by Lawrence *et al.* (1991) in terms of vorticity dynamics. When $d \neq 0$, the shear layers in each fluid give rise to two horizontal trains of corotating vortices above and below the interface. If J is sufficiently small, i.e. for strong shear or weak density differences, vortices on each side of the interface merge in pairs to form a stationary Kelvin–Helmholtz vortex. If J is too large however, the density discontinuity acts as a barrier to prevent merging and both arrays keep their identity, travelling at the local speed of the basic flow in each fluid. Two trains of counter-propagating Holmboe waves are then obtained as

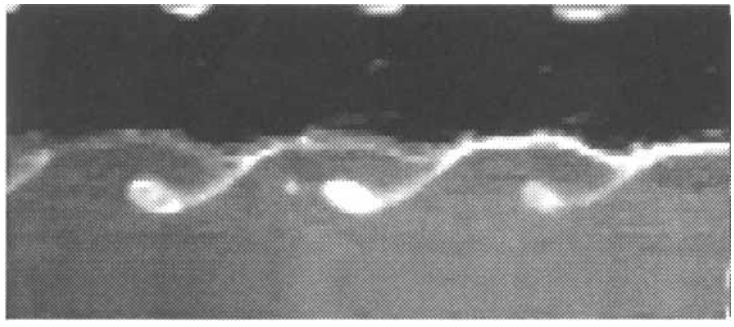

FIGURE 11. Flow visualization of vortex train in lower fluid obtained by dropping fluorescein dye on the interface prior to tilting the tank. Holmboe wave regime. Fluid set 2, $\Delta U_m^* = 12$ cm s^{-1}, $\lambda_f^* = 3$ cm, $t^* = 2$ s.

sketched on figure 10. The existence of vortical structures within each fluid can be verified experimentally by dropping fluorescein dye on the interface before tilting the tube (figure 11). As waves begin to propagate on the interface, dye is collected into 'beautiful' vortices in the lower fluid, which travel at the same speed as one of the interfacial waves. A parallel array of vortices moving in the opposite direction also exists in this case in the upper layer, but it cannot be visualized with this technique since fluorescein dye does not mix with the upper fluid.

In order to quantitatively compare the dynamics of the observed Holmboe waves with the results of the linear instability analysis presented in §4.1, it is first necessary to choose an appropriate pair of working fluids. As shown on figure 9(*a*), a typical run with fluid set 1 leads to relatively rapid variations of the scaled thickness d and to an undesirable transition from the Kelvin–Helmholtz regime into the Holmboe regime. The properties of fluid set 2 were 'taylored' to proceed directly from the stable domain into the Holmboe domain and to minimize variations of the scaled thickness d. As indicated in table 1, the viscosities of fluid set 2 are of the same order of magnitude as those of set 1 but the surface tension and asymmetry parameter β are much smaller. The capillary lengthscale L^* is therefore smaller and the dimensionless thickness $d = d^*/L^*$ larger. As seen from the curves marked with circles on figure 9(*b*), a typical run exhibits a direct transition to the Holmboe instability. Furthermore, the larger values of d lead to a lower value of J_c (see figure 7) and consequently to a higher critical velocity difference ΔU_c^*. The first observable deformation of the interface therefore appears at a later stage in the experiment, when the thickness $d^* \sim (\nu_2^* t^*)^{\frac{1}{2}}$ experiences only mild variations. The quasi-steady approximation may then be expected to hold. Finally one notes from table 1 that fluid set 2 yields a very small value of the asymmetry parameter β so that the theoretical analysis of §4.1 is indeed relevant.

As seen from figure 12, the resulting spatio–temporal diagram displays a striking chessboard pattern formed by the superposition of two counter-propagating Holmboe waves of equal amplitude. In contrast to the corresponding plot pertaining to fluid set 1 (figure 3), propagating disturbances prevail right at the onset of the instability.

In order to compare the experimental results with the linear instability analysis, a particular value of the slowly varying parameter d must be selected. In a typical experimental run with fluid set 2, d varies by less than 20% between the appearance of the first deformation and the end of the experiment. In the linear range, one may therefore consider d as approximately constant and equal to the value d_c at the onset when the experimental path crosses the marginal stability curve in the (d, J)-plane on figure 9(*b*). But, as seen from figure 9(*b*), d_c also changes from experimental run to

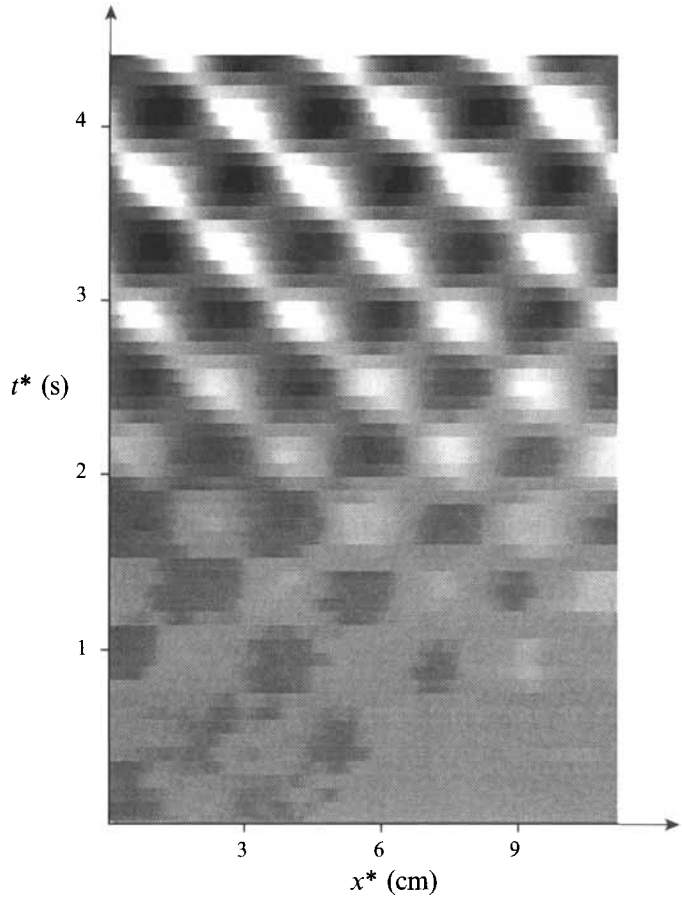

FIGURE 12. Spatio–temporal x^*–t^* diagram of the interface deformation. Fluid set 2, $\Delta U_m^* = 14$ cm s^{-1}, $\lambda_f^* = 3.7$ cm. The tube is brought back to its horizontal position at $t^* = 0.72$ s.

experimental run as the nominal value of the modified Richardson number J_m is varied. In the range that has been explored $0.2 \leqslant J_m \leqslant 0.4$, which corresponds to the velocity differences $5 \leqslant \Delta U^* \leqslant 14$ cm s^{-1}, the maximum excursions of d_c do not exceed 10%. For simplicity, d_c^* was therefore kept constant in the stability calculations, at the mean value $d_c^* = 0.6$ cm, which corresponds to a scaled thickness of the diffusion layer $d_c = 1.9$. Linear theory then gives a threshold value $J_c = 0.355$ and a threshold wavenumber $k_c = 0.895$. Comparison of these predictions with unforced experiments turns out to be difficult. Large fluctuations in the measured critical wavenumber k_c and critical value J_c of the control parameter are observed. The wavenumber k_c appears to fluctuate between 0.5 and 1 when J_c varies from one experiment to another from 0.3 to 0.37. These fluctuations can be understood by following in the (k, J)-plane the path of the most amplified mode according to linear theory. Figure 13 reveals that, in the range of modified Richardson number that has been explored $(0.2 < J < 0.4)$, the most amplified wavenumber k_{ma} experiences wide variations, moving rapidly away from the critical value k_c when J decreases from its threshold value. This rapid shift of k_{ma} away from k_c explains the lack of a sharp natural wavelength selection mechanism to create a perfectly periodic deformation of the interface. Spatial forcing then appears to be essential in order to experimentally produce a periodic pattern, and to make

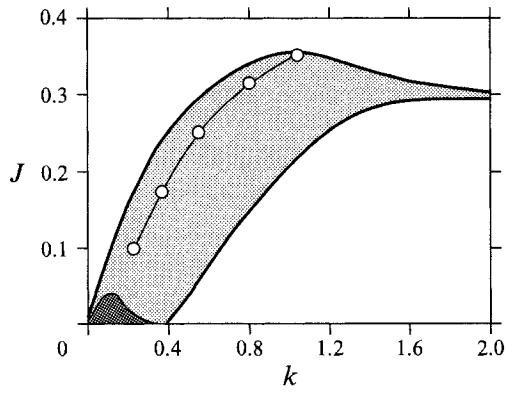

FIGURE 13. ○, Locus of the most amplified wavenumber k_{ma} in the (k, J)-plane, $d = 1.9$. The clear, shaded and dotted regions are defined as in figure 5.

quantitative comparisons with linear theory. In all the experimental runs with fluid set 2 to be reported below, the flow is spatially forced at the wavelength $\lambda_f^* = 3.7$ cm that corresponds to a dimensionless wavenumber $k_f = 0.54$.

Theoretical predictions of the variations of the real and imaginary parts, c_r and c_i, of the complex phase velocity are shown on figure 14(*a*, *b*) as a function of modified Richardson number J. The corresponding experimental points indicated by circles are obtained in the following manner. A spatial Fourier transform is first applied to the interface elevation at each time step, every 0.08 s, and the time history of the complex Fourier amplitude $A(t)$ at the forcing wavenumber is extracted. The temporal variations of the amplitude $|A|$ and phase ϕ of the forcing wavenumber component $A(t)$ are then obtained, as illustrated on figure 15(*a*). This procedure is equivalent to performing a sinusoidal fit of the interface deformation at the forcing wavenumber, $|A|(t)$ representing the amplitude of the sine function and $\phi(t)$ its phase. The temporal Fourier transform of the complex amplitude $A(t)$ is then found to present well-defined peaks at the frequencies ω and $-\omega$ of each propagating wave. Half of the frequency spectrum is used to reconstruct the temporal signal of a single propagating wave as illustrated on figure 15(*b*, *c*). The slope of the phase then yields the phase velocity c_r whereas the evolution of the amplitude provides a measure of the corresponding temporal growth rate from which the amplification factor c_i may be extracted. Thus one is able to separate right- and left-running waves from the original signal.

Satisfactory agreement is obtained between theory and experiment for the phase velocity and growth rate variations with J as shown on figure 14(*a*, *b*). Experimental points corresponding to right-moving (respectively left-moving) waves are indicated by circles (respectively squares). Error bars on the growth rate factor are essentially due to the image sampling frequency that is slightly too small compared to the characteristic evolution time of the instability. The small asymmetry observed between right- and left-propagating waves most likely arises from non-Boussinesq effects. Given all these uncertainties, the present results demonstrate that a simple theoretical analysis is capable of predicting the onset and the growth of the instability, as well as its propagative nature. Some of the limitations of the model are examined below.

We recall that the linear instability analysis of §4.1 is purely inviscid. One should therefore discuss whether the effects of viscous dissipation on the development of the instability are indeed negligible. For fluid set 2, the Reynolds number Re_m based on U_m^* and the quasi-stationary value d_m^* of the thickness is, for a typical run, of order

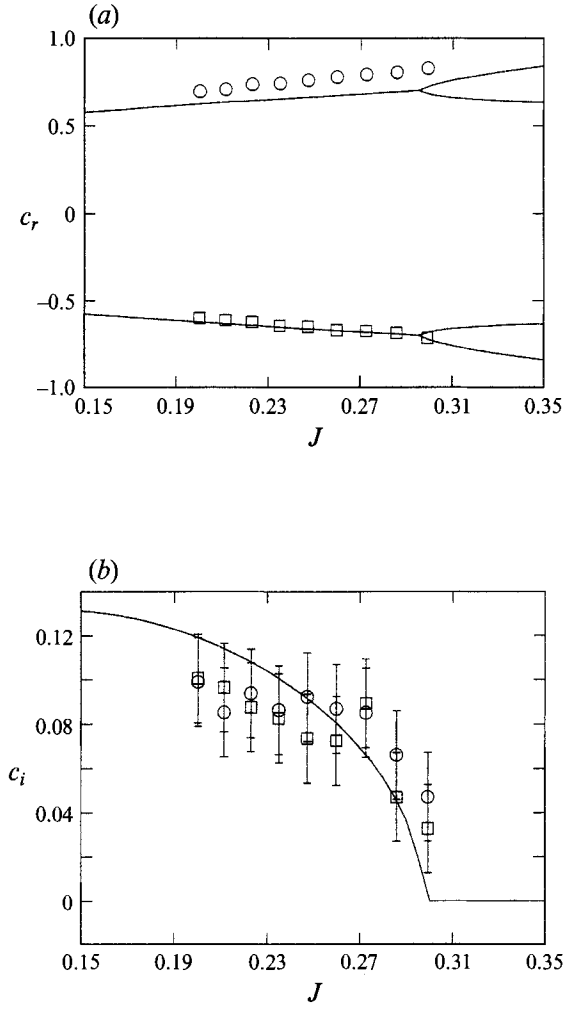

FIGURE 14. Variations of (*a*) the real part c_r and (*b*) imaginary part c_i of the complex phase velocity as a function of the Richardson number J for symmetric velocity profile. The wavenumber is fixed at $k = 0.54$. Continuous curves, theoretical predictions; ○, experimental data points for right-moving wave; □, experimental data points for left-moving wave. Fluid set 2, $d = 1.9$, $\beta = 0$.

$Re_m = 120$. Early calculations by Betchov & Szewczyk (1963) have indicated that viscous growth rates rapidly converge to corresponding inviscid values in the case of homogeneous mixing layers above a Reynolds number of the order of 50. Indeed the experimentally measured growth rates of Ho & Huang (1982) in a spatially developing homogeneous mixing layer at a Reynolds number of the order 38 (with the present choice of lengthscale and velocity scale) compare very favourably with inviscid stability calculations (figure 22 in Ho & Huang). It therefore appears legitimate to neglect viscous dissipation effects on the evolution of the waves, at least as a dominant approximation. One notes, however, that finite-Reynolds-number effects may have a subtle influence on the nature of the most amplified wave in continuously stratified mixing layers as demonstrated by Smyth & Peltier (1990). These authors have shown that the fastest growing wave can be three-dimensional below a Reynolds number of the order of 400. Unfortunately these results cannot be directly extrapolated to the

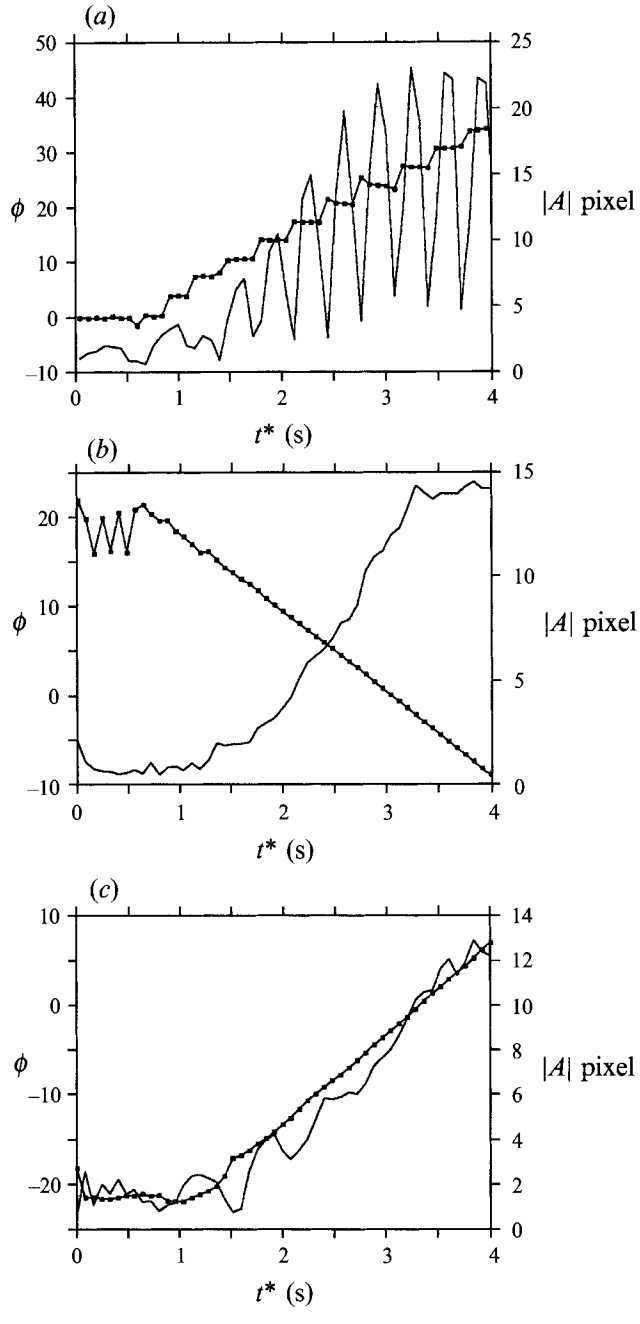

FIGURE 15. Illustration of the procedure used to extract the phase velocity c_r and growth factor c_i from the complex amplitude $A(t)$ at the forcing wavenumber. Fluid set 2, $\Delta U_m^* = 14$ cm s^{-1}, $\lambda_f^* = 3.7$ cm. ——, Amplitude $|A(t)|$; ■, phase $\phi(t)$. (*a*) Amplitude and phase variations of total forcing wavenumber component; (*b*) amplitude and phase variations of left-running wave; (*c*) amplitude and phase variations of right-running wave.

present discontinuous interface situation. All our visual observations indicate that the motion of the interface gives rise to wave fronts that are normal to the axis of the tube and no significant three-dimensional phenomena have been detected: the diameter of the tube is small enough that all three-dimensional disturbances are quenched.

In the linear stability analysis, it is assumed that the basic flow consists of two streams which are unbounded both in the horizontal and vertical directions. In the experiment, the thickness of each layer varies from a tube radius to zero in a direction parallel to the wavefronts. No significant three-dimensional distortion was induced by the finite geometry: the fluorescein dye line of figure 8 remains in the same vertical plane throughout the duration of the experiment. Lateral boundaries are also known to be stabilizing. According to Thorpe (1969, §2.2), the threshold of instability is the same as for the infinite-depth case when the thickness h^* of each fluid layer exceeds $3L^*$. This constraint corresponds in our case to a minimum height $h^* \approx 1$ cm. Such a value is reached only near the contact line where the interface intersects the wall of the tube.

4.3. *Asymmetric velocity profile: theoretical results*

When the kinematic viscosities of each fluid are not the same ($\delta \neq 1$), the asymmetry parameter β is not zero and the velocity profile looses its symmetry.

Odd powers of c in the dispersion relation (4) are no longer identically zero. Consequently, if c is a solution, $-c$ is not a solution although eigenvalues still appear as complex-conjugate pairs in the complex (c_r, c_i)-plane. This partial breaking of symmetry implies that the properties of right- and left-running waves are no longer identical. The effect of β on the mode diagram in the (k, J)-plane is illustrated on figure 16 for a finite value of d. Corresponding loci of the roots of (4) as J gradually decreases to zero on the vertical line $k = 1$ are displayed on figure 17. The most noteworthy difference between the symmetric profile $\beta = 0$ (figures 16*a* and 17*a*) and the asymmetric profile, for instance $\beta = 0.03$ (figures 16*b* and 17*b*), is the emergence of a domain with a single unstable propagating mode as indicated by the hatched regions on figure 16(*b*, *c*). As the marginal stability boundary is crossed from above, a single propagating mode becomes unstable when $\beta \neq 0$ (hatched band on figure 16*b*), whereas two counter-propagating Holmboe waves simultaneously become unstable when $\beta = 0$ (shaded region on figure 16*a*). As seen from figure 17(*b*), the propagation velocity c_r of the first unstable wave to appear is negative, i.e. opposite to the fluid velocity β at the interface. According to (3), the interface velocity β is in the same direction as the fluid velocity of the more viscous fluid (see also figure 4). We can therefore conclude that *the first destabilized wave moves in the same direction as the less viscous fluid, where the diffusion layer is thinner*. This last result appears to be a little surprising when compared to the conclusion reached by Lawrence *et al.* (1991) in the case of an asymmetrically sheared density interface without surface tension. These authors find that the first destabilized mode at a fixed wavenumber is associated with the thicker diffusion layer. However, a 'unified' criterion accounting for both flow situations takes the following form: the first destabilized wave moves in the same direction as the fluid that experiences the largest shear across the diffusion layer.

As the modified Richardson number J is gradually decreased at a finite value of β (figure 17*b*, *c*), a single collision of the real eigenvalues first takes place on the negative real axis which signals the appearance of a single unstable left-running wave. When J crosses into the shaded domain, the right-running wave also becomes unstable as two real eigenvalues collide on the positive real axis. In this range of modified Richardson numbers, there exists a pair of counter-propagating waves with unequal velocities c_r^+ and c_r^-. According to (4), both velocities are related by

$$c_r^+ + c_r^- = \tfrac{1}{2}n_3 = -\beta.$$

For lower values of J, the right-running wave is stabilized as the corresponding complex-conjugate pair of eigenvalues experiences a final embrace on the real axis.

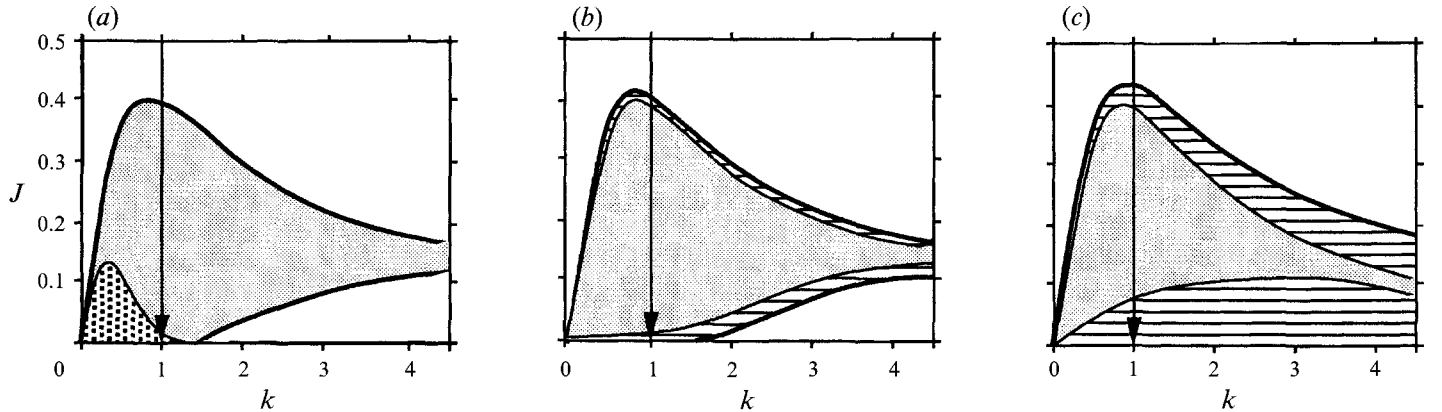

FIGURE 16. Stability diagram of piecewise-linear model in the (wavenumber k, Richardson number J)-plane for different values of the asymmetry parameter β. $d = 0.5$. Clear regions: neutrally stable modes ($c_r \neq 0$; $c_i = 0$); dotted regions: stationary unstable Kelvin–Helmholtz modes ($c_r = 0$; $c_i > 0$); shaded regions: pair of counter-propagating unstable modes ($c_r \neq 0$; $c_i > 0$); hatched regions: single propagating unstable mode ($c_r \neq 0$; $c_i > 0$). Thicker curve: marginal stability boundary, (*a*) $\beta = 0$; (*b*) $\beta = 0.03$; (*c*) $\beta = 0.3$.

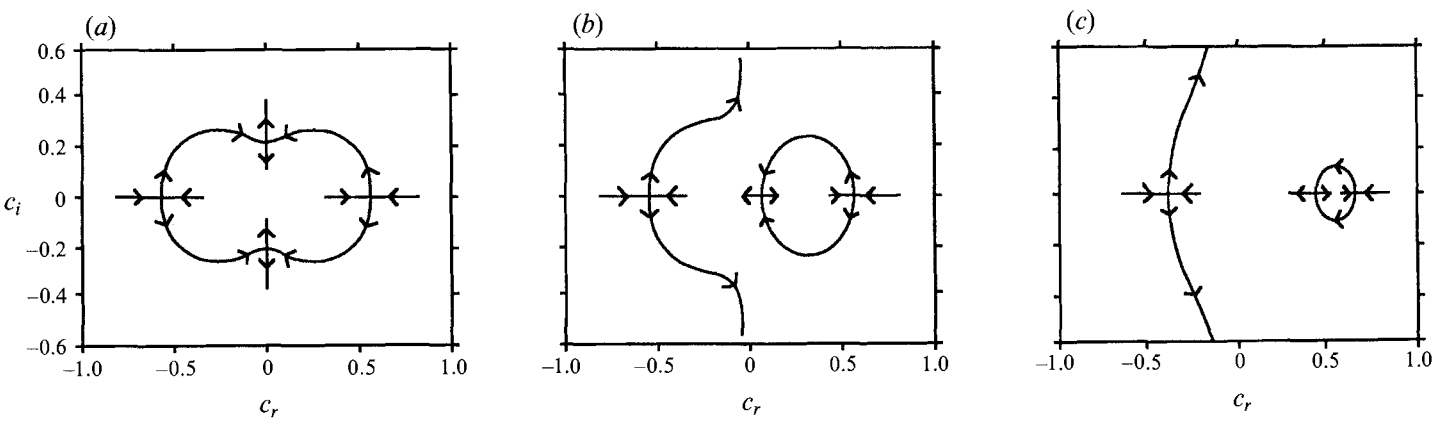

Figure 17. Loci of eigenvalues in complex (c_r, c_i)-plane as Richardson number J is decreased along vertical path indicated on figure 16, for different values of the asymmetry parameter β. (*a*) $\beta = 0$; (*b*) $\beta = 0.03$; (*c*) $\beta = 0.3$. Arrows indicate the direction of migration of the eigenvalues as J is lowered.

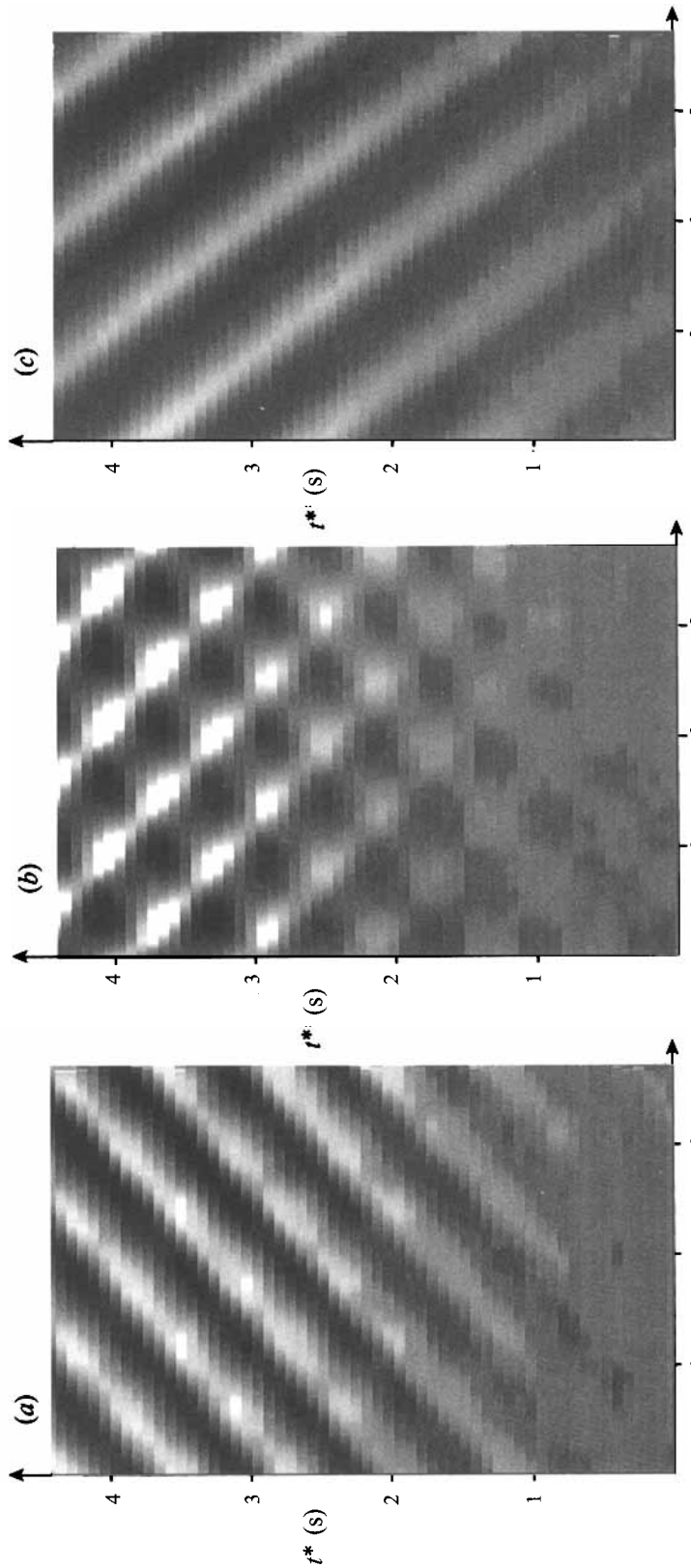

FIGURE 18. Spatio–temporal x^*–t^* diagram of interface elevation. $\Delta U_m^* = 12$ cm s^{-1}, $\lambda_y^* = 3.7$ cm. (*a*) $\beta = -0.09$, (*b*) $\beta = 0.007$, (*c*) $\beta = 0.14$. The tube is brought back to its horizontal position at $t^* = 0.5$ s.

Increasing the asymmetry parameter β is seen to reduce the range of modified Richardson numbers in which the right-running wave is unstable. Thus, waves moving in the direction of the more viscous fluid are gradually stabilized as its viscosity is enhanced. Finally we note that left-running waves travelling in the same direction as the less viscous fluid are more and more unstable (larger c_i) when J approaches zero, but their propagation velocity c_r gradually decreases to zero.

In the symmetric case (§4.1), one could distinguish unambiguously between Kelvin–Helmholtz modes defined by the stationary condition $c_r = 0$ and Holmboe modes defined by the propagating condition $c_r \neq 0$. Such a sharp distinction is no longer tenable when the symmetry of the basic velocity profile is broken ($\beta \neq 0$). A small non-zero value of β (figure 17*b*) is seen to eliminate the two collisions of eigenvalues taking place on the imaginary axis for $\beta = 0$ (figure 17*a*). As a result the Kelvin–Helmholtz domain (dotted area in figure 16*a*), in which the eigenvalues are purely imaginary, disappears in figure 16(*b*). In the strict sense, stationary waves are then obtained only in the limit $J = 0$. It can be concluded that the slightest asymmetry blurs the boundary between the Kelvin–Helmholtz and Holmboe regimes. We have therefore avoided the use of this terminology in this section.

4.4. *Asymmetric velocity profile: comparison with experiments*

The theoretical considerations outlined above indicate that small differences in the kinematic viscosities of the two fluids have subtle effects on the nature of the instability close to onset. In particular, the observed asymmetry between right- and left-running waves on the spatio–temporal diagram of figure 3 can now be understood. The properties of fluid set 1 listed in table 1 yield the value $\beta = 0.20$ of the asymmetry parameter and one should expect predominantly left-running waves moving in the same direction as the less-viscous water, in qualitative agreement with observations.

The asymmetry parameter β of fluid set 2 can be controlled by adjusting the viscosity of the upper fluid through variations in the concentration of silicone oil V100 in the mixture. Different x^*–t^* diagrams are then obtained as illustrated on figure 18. Figure 18(*a*) corresponds to a mixture of 7 % silicone oil and 93 % kerosene (fluid set 3) so that $\beta = -0.09$ and predominantly right-moving waves are observed. When $\beta = 0.007$, with a mixture of 12 % silicone oil and 88 % kerosene fluid (fluid set 2), two counter-propagating waves of equal amplitude are generated (figure 18*b*). Finally, when the upper fluid is made of 20 % silicone oil and 80 % kerosene, $\beta = 0.14$ and left-running waves are the only ones observed (figure 18*c*). Thus, in agreement with the theoretical results of §4.3, the instability mechanism selects propagating waves moving in the same direction as the less-viscous fluid. Measured values of the phase velocity and growth factor for fluid set 3 and $\beta = -0.09$ are compared with the predictions of linear theory on figure 19(*a*, *b*). As in the symmetric case, satisfactory agreement is obtained between the theory and the experiments, therefore demonstrating that the effects of asymmetry are also well described by a simple theoretical model based on a piecewise-linear profile.

5. Conclusions

The interface separating two streams of immiscible fluids has been shown, from a linear stability analysis, to become unstable below a well-defined value of a modified Richardson number when surface tension effects are included. If the velocity profile is odd with respect to the location of the density discontinuity and the evolution of the perturbation is strictly inviscid, the problem is invariant under both space and time

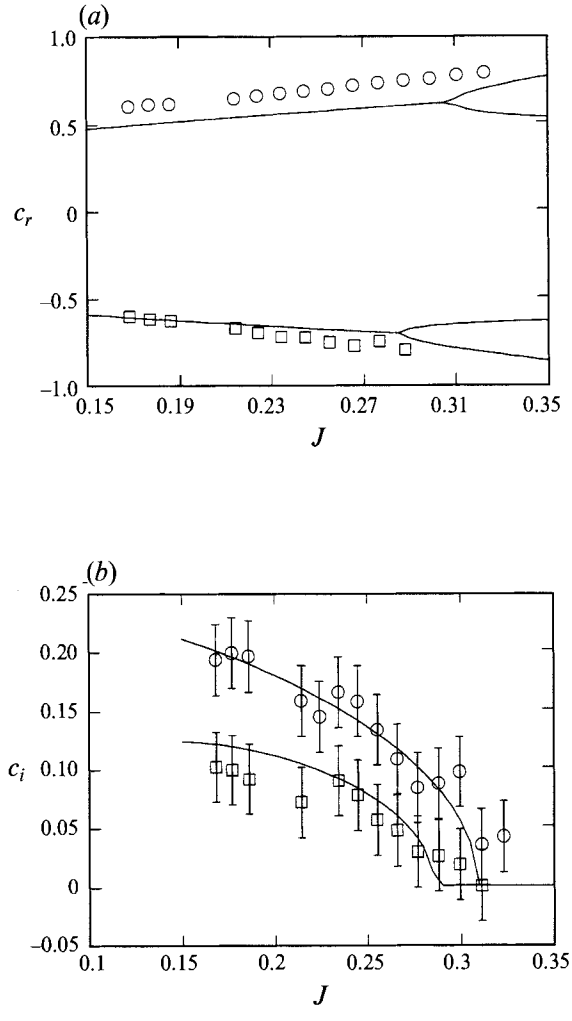

FIGURE 19. Variations of (*a*) the real part c_r and (*b*) imaginary part c_i of the complex phase velocity as a function of the Richardson number J for asymmetric velocity profile. The wavenumber is fixed at $k = 0.51$. Continuous curves, theoretical predictions; ○, experimental data points for right-moving wave; □, experimental data points for left-moving wave. Fluid set 3, $d = 1.4$, $\beta = -0.09$.

reflections, $x \to -x$ and $t \to -t$. In this situation, as the modified Richardson number crosses through the threshold value from above, the onset of instability is signalled by one of two possible scenarii in the (c_r, c_i)-plane of the complex phase velocity c. If the thickness of the velocity profile is zero, i.e. in the vortex sheet limit, two real values of c collide at the origin to give rise to a single pair of stationary amplified and decaying Kelvin–Helmholtz modes. As soon as the thickness of the velocity profile becomes non-zero, this scenario becomes invalid. Instead, two sets of real values of c collide at finite and opposite values of the propagation velocity to give rise to two pairs of counter-propagating amplified and decaying Holmboe modes. Amplified and decaying stationary Kelvin–Helmholtz modes are only recovered at lower Richardson numbers. Experimental observations and measurements in a tilting tank apparatus with two fluids of approximately equal kinematic viscosities have shown that the threshold values of the velocity difference and wavenumber are reasonably well predicted by the

model. Furthermore, the onset of instability is characterized by the appearance of counter-propagating Holmboe waves with phase speeds and growth factors as predicted by the finite-thickness analysis. Thus, the generation of diffusive layers on either side of the interface drastically alters the qualitative nature of the instability. It is only in the accelerating shear flow configuration (constant values of the tilting angle), that one may hope to remain in a domain with negligible diffusive-layer thicknesses and to observe stationary Kelvin–Helmholtz perturbations. It is worth mentioning that counter-propagating waves have also been encountered near onset in other fluid systems displaying the reflectional symmetry $x \to -x$, for instance convecting layers of binary fluid mixtures (Kolodner *et al.* 1986; Surko & Kolodner 1987). In the latter case the disturbance field is strongly dissipative with no invariance under time reflections so that instability arises by simple crossing of two eigenvalue branches into the upper half-plane $c_i > 0$ at symmetrically located points on the c_r-axis.

When the velocity profile displays some asymmetry, the reflectional invariance $x \to -x$ is broken and the linear stability results indicate that only a single propagating wave appears at the critical value of the modified Richardson number. The unambiguous distinction between Kelvin–Helmholtz and Holmboe modes is then lost and, at very low modified Richardson numbers, one gradually approaches the limit of stationary Kelvin–Helmholtz disturbances. Experiments carried out in sets of fluids with different kinematic viscosities fully confirm these predictions qualitatively and quantitatively: the first destabilized wave moves in the same direction as the stream of less-viscous fluid. The dominant propagation direction or lack thereof can be manipulated by altering the respective fluid viscosities. It can be concluded from this study and the earlier investigation of Pouliquen *et al.* (1992) that Thorpe's original set-up can be used to advantage in a spatially forced configuration to understand the spatio–temporal behaviour of Holmboe waves at a density discontinuity.

The authors have benefitted from fruitful and stimulating discussions with Hugues Chaté, Stéphane Douady, Vincent Hakim, Greg Lawrence, Paul Manneville, Larry Redekopp, Maurice Rossi, Patrick Tabeling, and Stéphane Zaleski. The experimental portion of this study would not have been possible without the technical assistance and joie de vivre of Antoine Garcia. Special thanks go to François Sicoli for helping us in measuring the surface tension. Many long and spirited exchanges have also taken place with Buck Danny and his gang at Patuxent River Air Force Base, Alaska.

The financial support of the Direction des Recherches, Etudes et Techniques (DRET) of the French Ministry of Defense under Grant 90-040 and of the Direction des laboratoires (Ecole Polytechnique) is gratefully acknowledged.

REFERENCES

Balsa, T. F. 1987 On the spatial instability of piecewise linear free shear layers. *J. Fluid Mech.* **174**, 553–563.

Betchov, R. & Szewczyk, A. 1963 Stability of a shear layer between parallel streams. *Phys. Fluids* **6**, 1391–1396.

Browand, F. K. & Winant, C. D. 1973 Laboratory observations of shear layer instability in a stratified fluid. *Boundary-Layer Met.* **5**, 67–77.

Delisi, D. & Corcos, G. M. 1973 A study of internal waves in a wind tunnel. *Boundary-Layer Met.* **5**, 121–137.

Drazin, P. G. & Howard, L. N. 1966 Hydrodynamic stability of parallel flow of inviscid fluids. *Adv. Appl. Mech.* **9**, 1–89.

Drazin, P. G. & Reid, W. H. 1981 *Hydrodynamic Stability*. Cambridge University Press.

HAZEL, P. 1972 Numerical studies of the stability of inviscid parallel shear flows. *J. Fluid Mech.* **51**, 39–62.

HO, C. M. & HUANG, L. S. 1982 Subharmonics and vortex merging in mixing layers. *J. Fluid Mech.* **119**, 443–473.

HO, C. M. & HUERRE, P. 1984 Perturbed free shear layers. *Ann. Rev. Fluid Mech.* **16**, 365–424.

HOLMBOE, J. 1962 On the behavior of symmetric waves in stratified shear layers. *Geofys. Publ.* **24**, 67–113.

HOWARD, L. N. & MASLOWE, S. A. 1973 Stability of stratified shear flows. *Boundary-Layer Met.* **4**, 511–523.

KOLODNER, P., PASSNER, A., SURKO, C. M. & WALDEN, R. W. 1986 Onset of oscillatory convection in a binary fluid mixture. *Phys. Rev. Lett.* **56**, 2661–2624.

KOOP, C. G. & BROWAND, F. K. 1979 Instability and turbulence in a stratified fluid with shear. *J. Fluid Mech.* **93**, 135–159.

LAWRENCE, G. A., BROWAND, F. K. & REDEKOPP, L. G. 1991 The stability of a sheared density interface. *Phys. Fluids* A **3**, 2360–2370.

LAWRENCE, G. A., LASHERAS, J. C. & BROWAND, F. K. 1987 Shear instabilities in stratified flow. *Proc. Third Intl Symp. on Stratified Flows, February 2–5, 1987, Pasadena, California.*

MASLOWE, S. A. & KELLY, R. E. 1971 Inviscid instability of an unbounded heterogeneous shear layer. *J. Fluid Mech.* **48**, 405–415.

MASLOWE, S. A. & THOMPSON, J. M. 1971 Stability of a stratified free shear layer. *Phys. Fluids* A **14**, 453–458.

MAXWORTHY, T. & BROWAND, F. K. 1975 Experiments in rotating and stratified flows: oceanographic applications. *Ann. Rev. Fluid Mech.* **7**, 273–305.

POULIQUEN, O., CHOMAZ, J. M., HUERRE, P. & TABELING, P. 1992 Wavenumber selection and phase solitons in spatially forced temporal mixing layers. *Phys. Rev. Lett.* **68**, 2596–2599.

REYNOLDS, O. 1883 An experimental investigation of the circumstances which determine whether the motion of water shall be direct or sinuous, and of the law of resistance in parallel channels. *Phil. Trans. R. Soc. Lond.* **174**, 935–985.

SCOTTI, R. S. & CORCOS, G. M. 1972 An experiment on the stability of small disturbances in a stratified shear layer. *J. Fluid Mech.* **52**, 499–528.

SMYTH, W. D., KLAASEN, G. P. & PELTIER, W. R. 1988 Finite amplitude Holmboe waves. *Geophys. Astrophys. Fluid Dyn.* **43**, 181–222.

SMYTH, W. D. & PELTIER, W. R. 1989 The transition between Kelvin–Helmholtz and Holmboe instability: an investigation of the overreflection hypothesis. *J. Atmos. Sci.* **46**, 3698–3720.

SMYTH, W. D. & PELTIER, W. R. 1990 Three-dimensional primary instabilities of a stratified dissipative, parallel flow. *Geophys. Astrophys. Fluid Dyn.* **52**, 249–261.

SMYTH, W. D. & PELTIER, W. R. 1991 Instability and transition in finite-amplitude Kelvin–Helmholtz and Holmboe waves. *J. Fluid Mech.* **228**, 387–415.

SURKO, C. M. & KOLODNER, P. 1987 Oscillatory traveling-wave convection in a finite container. *Phys. Rev. Lett.* **58**, 2055–2058.

THORPE, S. A. 1968 A method of producing a shear flow in a stratified fluid. *J. Fluid Mech.* **32**, 693–704.

THORPE, S. A. 1969 Experiments on the instability of stratified shear flows: immiscible fluids. *J. Fluid Mech.* **39**, 25–48.

THORPE, S. A. 1973*a* Turbulence in stably stratified fluids: a review of laboratory experiments. *Boundary-Layer Met.* **5**, 95–119.

THORPE, S. A. 1973*b* Experiments on instability and turbulence in a stratified shear flow. *J. Fluid Mech.* **61**, 731–751.

WEISSMAN, M. A. 1979 Non linear wave packets in the Kelvin–Helmholtz instability. *Phil. Trans. R. Soc. Lond.* A **290**, 639–685.